RESEARCH ARTICLE

NANO · MICRO small
www.small-journal.com

Effect of Ni-Doping on the Optical, Structural, and Electrochemical Properties of Ag_{29} Nanoclusters

Abdullah A. A. Ahmed, Shana Havenridge, Koustav Sahoo, Loknath Thapa, Ananya Baksi, Guido H. Clever, Heshmat Noei, Mona Kohantorabi, Andreas Stierle, C. Retna Raj, Wolfgang J. Parak, Christine M. Aikens,* and Indranath Chakraborty**

Atomically precise metal nanoclusters (NCs) can be compositionally controlled at the single-atom level, but understanding structure-property correlations is required for tailoring specific optical properties. Here, the impact of Ni atom doping on the optical, structural, and electrochemical properties of atomically precise 1,3-benzene dithiol (BDT) protected Ag_{29} NCs is studied. The Ni-doped Ag_{29} ($NiAg_{28}(BDT)_{12}$) NCs, are synthesized using a co-reduction method and characterized using electrospray ionization mass spectrometry (ESI MS), ion mobility spectrometry (IMS), and X-ray photoelectron spectroscopy (XPS). Only a single Ni atom doping can be achieved despite changing the precursor concentration. Ni doping in Ag_{29} NCs exhibits enhanced thermal stability, and electrocatalytic oxygen evolution reaction (OER) compared to the parent NCs. Density functional theory (DFT) calculations predict the geometry and optical properties of the parent and $NiAg_{28}(BDT)_{12}$ NCs. DFT is also used to study the systematic single-atom doping effect of metals such as Au, Cu, and Pt into Ag_{29} NCs and suggests that with Ni and Pt, the d atomic orbitals contribute to creating superatomic orbitals, which is not seen with other dopants or the parent cluster. The emission mechanism is dominated by a charge transfer from the ligands into the Ag core cluster regardless of the dopant.

1. Introduction

Atomically precise metal nanoclusters (NCs), consisting of an inner metal core and an outer metal-ligand shell, have received considerable attention due to their tuneable physicochemical properties.[1] Combining two or more metals to fabricate novel geometries and fundamental properties of metal NCs, thus fabricating alloy nanostructures, presents an attractive opportunity for nanoscience and nanotechnology.[2,3] Several articles have shown that bi-metallic NCs may offer significantly enhanced properties compared to the parent NCs due to the synergistic effects of the heteroatom(s).[4–12] The most common synthesis methods for doped NCs are galvanic exchange,[13] co-reduction,[14] intercluster reactions,[15] and ligand-induced conversion of bimetallic NCs to doped NC.[12] Depending on the metal atom and synthesis method,[4–12] the doping position in the NCs can be

A. A. A. Ahmed, W. J. Parak, I. Chakraborty
Center for Hybrid Nanostructures (CHyN) and Fachbereich Physik
Universität Hamburg
22607 Hamburg, Germany
E-mail: wolfgang.parak@uni-hamburg.de; indranath@iitkgp.ac.in

A. A. A. Ahmed
Department of Physics
Faculty of Applied Science
Thamar University
Dhamar 87246, Yemen

S. Havenridge, C. M. Aikens
Department of Chemistry
Kansas State University
Manhattan, KS 66506, USA
E-mail: cmaikens@ksu.edu

K. Sahoo, I. Chakraborty
School of Nano Science and Technology
Indian Institute of Technology Kharagpur
Kharagpur 721302, India

L. Thapa, C. R. Raj
Functional Materials and Electrochemistry Lab
Department of Chemistry
Indian Institute of Technology Kharagpur
Kharagpur 721302, India

A. Baksi, G. H. Clever
Department of Chemistry and Chemical Biology
TU Dortmund University
44227 Dortmund, Germany

H. Noei, M. Kohantorabi, A. Stierle
DESY NanoLab
Deutsches Elektronen Synchrotron (DESY)
22607 Hamburg, Germany

The ORCID identification number(s) for the author(s) of this article can be found under https://doi.org/10.1002/smll.202408096

DOI: 10.1002/smll.202408096

varied, which considerably influences their properties.[16] Doping in metal NCs is an effective strategy for enhancing their physicochemical properties. Numerous alloyed and doped NCs have been documented, particularly in relation to gold-based NCs.[7,8,17–19] Reports of doping Ag NCs have also risen significantly recently, mainly in the case of Ag_{29} NCs.[17,20–22]

Typically, the doped metal atoms can occupy the central core or the kernel shell of Ag NCs depending on several factors of the doping metals, including atomic size and the resultant geometric and electronic stability of the consequent doped NCs.[19,23–25] For example, Au, Pt, and Pd were found in the central core, whereas Cu was found in the kernel shell for the case of doped-$Ag_{29}(BDT)_{12}(TPP)_4$ NCs (BDT: 1,3- benzene dithiol, TPP: triphenylphosphine).[26] Compared with the parent Ag NCs, the doped Au, Cu, Pt, and Pd atoms demonstrate enhanced stability and induce charge stripping, leading to various valence states.[19] A small but definite number of Au atoms has been used as dopants to enhance photoluminescence (PL) spectra and quantum yield by 26 times while increasing the ambient stability of Ag NCs[7,8] and has been used to yield an excellent catalyst in the electrochemical reduction of CO_2 to CO.[5] Introducing single Pt atoms in $Ag_{29}(BDT)_{12}(TPP)_4$ can change their electronic stability significantly, as their PL properties (such as enhanced quantum yield) are compared to the parent cluster.[6] $Ag_{17}Cu_{12}(BDT)_{12}(TPP)_4$ has been used as a catalyst for a three-component coupling reaction (i.e., A^3 coupling where an alkyne, an aldehyde, and an amine can be coupled), and it shows enhanced catalytic performances over $Ag_{29}(BDT)_{12}(TPP)_4$ NCs.[3] Moreover, the doped NCs ($Ag_{17}Cu_{12}$) exhibited thermal stability compared to the parent nanoclusters (Ag_{29} NCs) under vacuum/air. Ion mobility mass spectrometry revealed that the collision cross section (CCS) of $[Cu_xAg_{29-x}(BDT)_{12}]^{3-}$ decreases linearly with the exchange of each Ag/Cu; DFT of NCs (after removal of TPP) with CCS calculations have been used to find the most stable isomers of NCs.[27] Several other groups have studied single metal doped Ag_{29} NCs and found that the Pt or Pd atoms occupy the icosahedral core rather than the stacking motifs, similar to $PtAg_{28}$.[12,28,29] Pradeep et al. have synthesized $NiAg_{28}$ NCs from $NiAg_{24}(DMBT)_{18}$ NCs (DMBT: 2,4-dimethylbenzenethiol) via a ligand exchange-induced core transformation method.[30]

Research into effective, affordable, and environmentally friendly alternative energy conversion technologies has intensified due to the growing demand for energy and environmental sustainability.[31] As a result, developing renewable energy technologies that include high-quality catalysts for the oxygen evolution reaction (OER) is crucial. Also, a promising clean, renewable energy technology is the electrocatalytic hydrogen evolution process (HER).[32] However, the lack of a homogeneous size, composition, structure, and chemical coordination environment in conventional nanocatalysts makes it challenging to find a clear relationship between structure and performance. Atomically precise NCs can be used as formidable model catalysts to understand the relationship between structure and catalytic capabilities. They are incredibly small and have a unique composition, a well-defined structure, and a homogeneous chemical environment at the atomic level.[33] Au and Au alloy NCs have been used to promote and catalyze HER,[34] while Ag-based NCs and their alloys showed a relatively weak ability to catalyze HER. In a recent report, the HER efficiency was boosted by core (Pt doping) and surface (external addition of 3d metals like Mn^{2+}) engineering of the Ag_{29} NCs.[35] Similarly, the doped $AuAg_{21}$ NCs exhibited enhanced utility as efficient oxygen reduction reaction (ORR) catalysts in alkaline solutions more than Ag_{22} NCs.[9] Moreover, noble metal NCs can significantly improve the performance of OER. Surprisingly, the $Au_{15}Ag_{23}$ NCs exhibit remarkable electrocatalytic properties for HER. Also, the $Au_{15}Ag_{23}$/NiFe-LDH catalyst (LDH: layered double hydroxide), when loaded in NiFe-LDH, exhibited exceptional electrocatalytic performance in OER. This is because NiFe-LDH and the $Au_{15}Ag_{23}$ NCs have electronic solid contact.[4] All these reports suggest that doping a metal atom in atomically precise NCs can significantly change their electrocatalytic properties, and 3d metals such as Ni might enhance their OER performance better than other noble metals.

Herein, we report the synthesis of $NiAg_{28}(BDT)_{12}$ NC via a direct co-reduction synthesis approach. The successful formation of $NiAg_{28}(BDT)_{12}$ NCs was confirmed by electrospray ionization mass spectrometry (ESI MS), ion mobility spectrometry (IMS), and X-ray photoelectron spectroscopy (XPS). $[NiAg_{28}(BDT)_{12}]^{4-}$, similar to the parent cluster $[Ag_{29}(BDT)_{12}]^{3-}$, is best described as a quasi-spherical cluster with four tetrahedral symmetric positions.[29] The electrochemical catalytic performances of Ag_{29} and $NiAg_{28}$ NCs have been explored to recognize the Ni doping effect on the OER efficiency.

2. Results and Discussion

Bimetallic $NiAg_{28}(BDT)_{12}$ NCs have been synthesized via a co-reduction approach following a protocol explained in the experimental section (details can be found in Supporting Information). The ESI MS spectrum of the Ag_{29} NCs exhibits the characteristic peaks in the negative ion mode with a 3^- charge state, as shown in Figure S1A (Supporting Information). The expansion of the 3^- charge state manifests that the calculated patterns match exactly the experimental isotopic patterns, as shown in Figure S1C (Supporting Information). The ESI MS spectrum reveals three peaks in the m/z = 1500–1800 Da range (at m/z = 1603.35, 1690.71, and 1778.08 Da.), which are separated by m/z = 87.4 Da, corresponding to $[Ag_{29}(BDT)_{12}]^{3-}$. Expansion of each peak exhibits a characteristic isotropic distribution where the peak separation corresponds to m/z = 0.33, which in turn corresponds to the 3^- charge state. These results are in good agreement with previous reports.[36–39] On the other hand, the ESI MS of $NiAg_{28}$ NCs presents an intense peak at m/z = 1190 with a 4^- charge state, corresponding to $[NiAg_{28}(BDT)_{12}]^{4-}$,[30] as shown in **Figure 1A**. The calculated and experimental isotopic MS patterns of all assigned peaks were explored in Figure S1 (Supporting Information). Besides $[NiAg_{28}(BDT)_{12}]^{4-}$ clusters, $[NiAg_{28}(BDT)_{12}]^{3-}$ was also observed in the ESI MS spectrum of $NiAg_{28}(BDT)_{12}$ NCs which corresponds to the peak at m/z = 1587 with 3^- charge state.

The change in the structure of $Ag_{29}(BDT)_{12}$ NCs associated with single Ni doping was explored by ion mobility spectrometry (IMS), as presented in Figure S2 (Supporting Information).

H. Noei, M. Kohantorabi, A. Stierle
Fachbereich Physik
University of Hamburg
20148 Hamburg, Germany

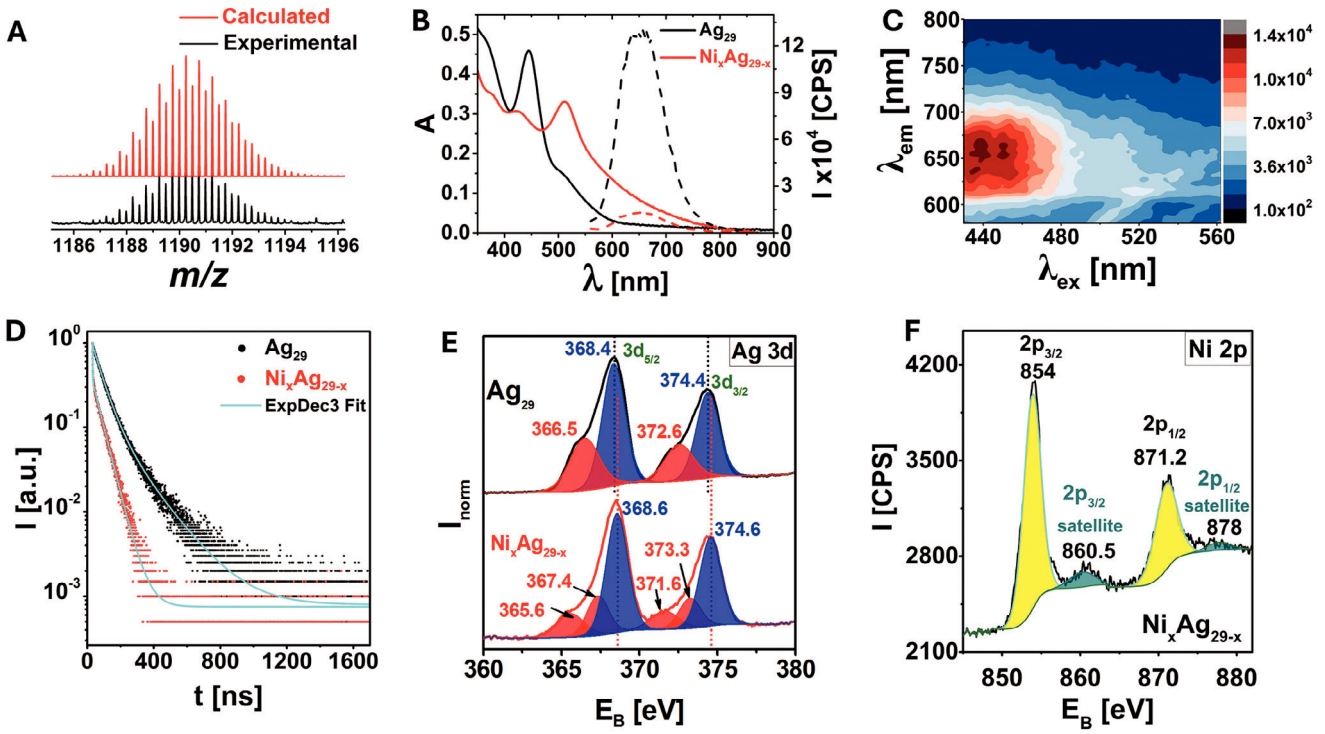

Figure 1. A) The calculated and experimental isotopic distributions of $[NiAg_{28}(BDT)_{12}]^{4-}$ charge states obtained from the ESI MS of the Ni-doped Ag_{29} NCs (a full range ESI MS is shown in Supporting Information). B) UV–vis absorption (solid) and PL (dashed) spectra of $NiAg_{28}$ (red trace) compared to Ag_{29} (black trace). C) 2D emission and excitation maps of $NiAg_{28}$ NCs. D) Luminescence decay curves at room temperature of Ag_{29} and $NiAg_{28}$ NCs, E) The XPS spectra of the Ag 3d peak for Ag_{29} NCs blueshifts slightly in Ni_xAg_{29-x} NCs, showing the intensity distribution of the binding energy $I_{norm}(E_B)$. F) XPS spectra of Ni 2p of the oxidative state of Ni^{2+} for Ni_xAg_{29-x} NCs. The bimetallic Ni_xAg_{29-x} NCs is referred to as AN2 sample, according to Table S1 (Supporting Information).

The collision cross section (CCS) confirms the reproducibility of the measured ion mobility of $Ag_{29}(BDT)_{12}$ NCs. The CCS value decreased by 1.7 Å^2 when Ni was substituted in $Ag_{29}(BDT)_{12}$ (the CCS values were found to be 479.2 and 477.5 Å^2 for the Ag_{29} and $NiAg_{28}$ NCs, respectively). The CCS values agree with published reports of doped NCs.[27,40] This refers to the fact that the van der Waals radius of the Ni atom (163 pm) is smaller than that of the Ag atom (172 pm). The metal NCs are also sensitive to the bonding situation, including metal–metal bonds and lengths. However, the central substitution of the Ag atom does not affect the overall geometry of the $Ag_{29}(BDT)_{12}$ system.[27] Therefore, based on the HRMS and IMS data, it is probable that the single Ni-atom is located in the central position in the icosahedral M_{13} units. We also have a peak at the higher side that the peak at the higher CCS may be related to the dynamic movement of the Ni atoms in and out within the cluster during measurement (see Figure S2, Supporting Information).

Density functional theory (DFT) calculations using the BP86-D3/DZP level of theory[41–44] in the Amsterdam Modeling Suite 2021.1[45] (see Supporting Information for full details) were used to complement the experiment to determine the most stable structure of 1–3 Ni atom dopants in the parent cluster. To decipher the correct position of the monodopant into the parent cluster, the Ni atom was placed in the center, core, "tetra" (referring to the tetrameric Ag connections), and "tri" positions (referring to the triangular Ag atoms in the Ag_3 triangles connected to the core) (**Figure 2**; Figures S11 and S12, Supporting Information). These optimized structures were compared, and the lowest energy structure was deemed the most stable. DFT calculations showed that the Ni atoms in $[Ni_2Ag_{27}(BDT)_{12}]^{5-}$ prefer to be in the center and staple position. $[Ni_3Ag_{26}(BDT)_{12}]^{6-}$ prefers to have one Ni atom in the center position, one in the core, and one in the staples (Table S5, Supporting Information). Furthermore, the optical properties change drastically, where 2 and 3 Ni atom dopants result in larger differences from the experiment, hinting that the experimentally observed cluster is a single atom doped cluster (Figure S13, Supporting Information). Different structures converged with 3^- and 4^- charge states for the monodoped cluster. These calculations found that the dopant prefers the center position with a charge state of 4^-, whereas it prefers the "tri" shell position with a charge state of 3^- as seen in Table S6 (Supporting Information). Different structural isomers could likely exist in the solution, resulting in a mixture of 3^- and 4^- overall-charged clusters. However, the theoretical analysis in the manuscript will be reported for the 4^- charged cluster as it exists in a closed shell singlet in its ground state.

It is important to note that despite the slight geometric changes between the monodoped NC and the parent, the electronic structure is drastically different. Both, $[Ag_{29}BDT_{12}]^{3-}$ and $[NiAg_{28}BDT_{12}]^{4-}$ have a superatom electron count of 8, giving rise to a S^2P^6 configuration. The molecular orbitals of $[Ag_{29}BDT_{12}]^{3-}$ are dominated by the p atomic orbital contributions from the

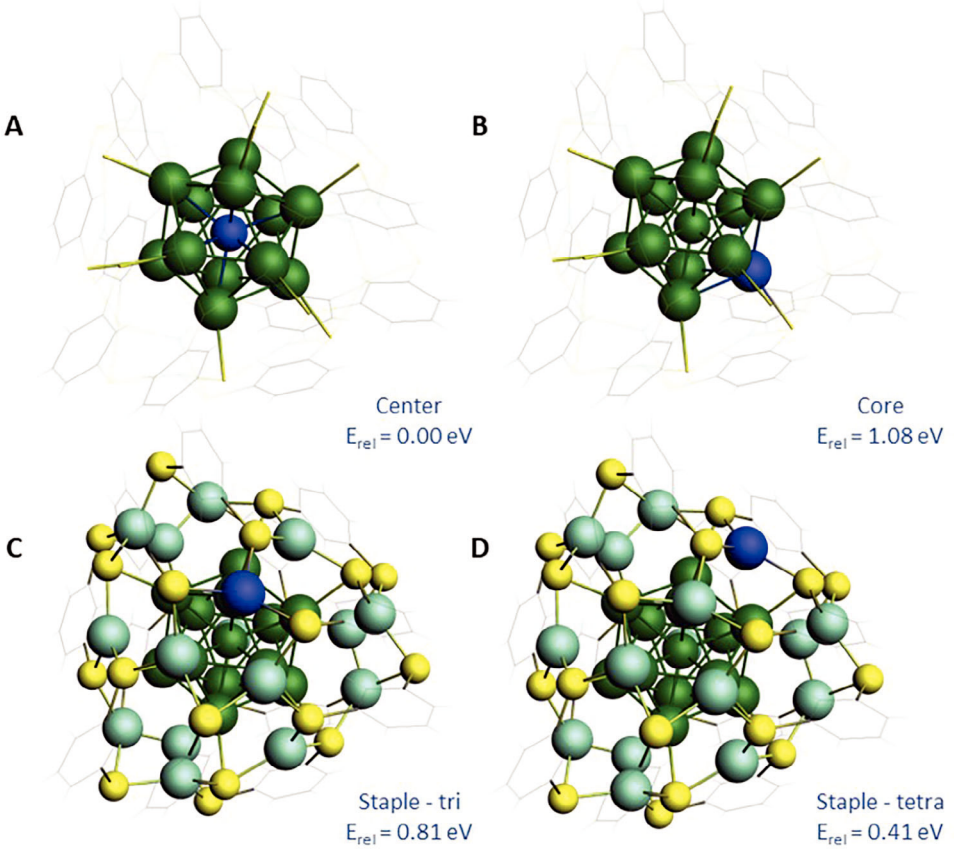

Figure 2. Dopant positions and relative energies at the BP86-D3/DZP level of theory in the A) Center B) Core C) Triangle "tri" position of the staple motif D) Tetrahedral "tetra" position of the staple motif. A full list of relative energies at each possible dopant position can be seen in Table S6 (Supporting Information). Color scheme: silver core = dark green, silver shell = light green, nickel = blue, sulfur = yellow, carbon = grey, hydrogen = white. The silver shell (A,B) and the ligands (A–D) are shown in wireframe for simplicity.

sulfur atoms, but a P superatomic orbital is not observed for the HOMO. With the $[NiAg_{28}BDT_{12}]^{4-}$ nanocluster, the sulfur p atomic orbitals still give a significant contribution, but the contribution from the d orbitals in Ni combine with the sp orbitals on the Ag core atoms to create a superatomic P orbital in the HOMO (H), H-1 and H-2 that is not observed in the parent cluster at this level of theory. The HOMO–LUMO (H-L) gaps in $[Ag_{29}BDT_{12}]^{3-}$ and $[NiAg_{28}BDT_{12}]^{4-}$ are 1.48 and 1.62 eV, respectively.

X-ray photoelectron spectroscopy (XPS) shows the existence of Ag, S, and C for pure Ag_{29} NCs (Figure S3, Supporting Information) and Ag, Ni, S, and C for bimetallic $NiAg_{28}$ NCs (Figure S4, Supporting Information). The binding energy of Ag $3d_{5/2}$ and $3d_{3/2}$ peaks in Ag_{29} NCs (Figure 1E, blue) are obtained at 368.4 and 374.4 eV, respectively, which are in good agreement with pure NCs.[6,46,47] After a Ni atom is substituted in the center of $Ag_{29}(BDT)_{12}$ to form $NiAg_{28}(BDT)_{12}$, the Ag 3d peaks blueshift to 368.6 and 374.6 eV corresponding to Ag $3d_{5/2}$ and $3d_{3/2}$ peaks, respectively, represented by vertical dashes in Figure 1E. Moreover, the main peak of Ni $2p_{3/2}$ and its satellite are at 854.0 and 860.5 eV, and the main peak of Ni $2p_{1/2}$ and its satellite are at 871.2 and 878.0 eV, respectively, in $NiAg_{28}$ NCs as shown in Figure 1F. This confirms that a doped NC is formed and exactly agrees with doped NCs.[30] In the XPS spectra of Ag 3d, two peaks in the Ag_{29} NCs at 366.5 and 372.6 eV and four peaks in the $NiAg_{28}$ NCs at 365.6, 367.4, 371.6, and 373.3 eV are assigned to Ag^+ (Figure 1E, red color), which may not have been reduced during cluster formation.[48,49]

The experimental optical absorption spectra of pure Ag_{29} NCs show an absorption peak at 445 nm while Ni-doped Ag_{29} manifests two peaks at 425 and 511 nm as shown in Figure 1B. PL spectra of $NiAg_{28}$ NCs were observed at 653 nm at the excitation wavelength of 450 nm; the PL spectrum displays a quenching effect of a factor of 9 compared to Ag_{29} NCs (Figure 1B). A series of emission spectra at different excitation wavelengths was recorded as a 2D map as presented in Figure 1C for $NiAg_{28}$ NCs. The 2D map of $NiAg_{28}$ NCs shows two excitation wavelengths at 439 and 520 nm and two emission wavelengths at 615 and 656 nm. On the other hand, the pure Ag_{29} NCs presented only one excitation wavelength at 445 nm and one emission wavelength at 652 nm. This is due to the presence of a Ni atom within Ag_{29} NCs. These results are in good agreement with what was reported by Pradeep and coworkers.[30,50,51] The room temperature luminescence lifetime was recorded for pure and Ni-doped Ag_{29} NCs as shown in Figure 1D. The average lifetime (τ_{av}) decreased from 96.1 ns for pure clusters to 52 ns for $NiAg_{28}$ NCs as seen in Table S3 (Supporting Information). This result is

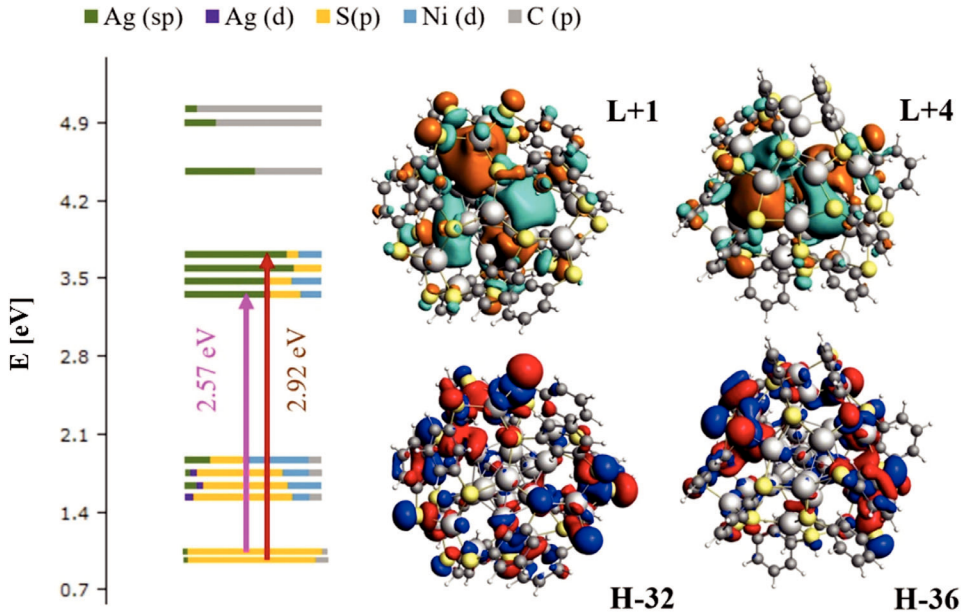

Figure 3. A) Atomic orbital contribution in selected Kohn–Sham molecular orbitals at the BP86-D3/DZP level of theory for $[NiAg_{28}BDT_{12}]^{4-}$ B) Molecular orbitals that make up the dominant transition in the first two peaks of the theoretical absorption spectrum at the BP86-D3/DZP level of theory for $[NiAg_{28}BDT_{12}]^{4-}$ (contour = 0.0135).

expected due to the lower intensity $NiAg_{28}$ NCs emission in PL measurements.

The decrease in PL intensity and lifetime in Ni-doped Ag_{29} NCs can be attributed to several factors. The doping of Ni at the central position of the Ag_{13} icosahedral core may increase the total angular momentum of the metal–metal intra-band transitions, thereby enhancing electron-phonon coupling, as reported in Pd-doped Au_{25} NCs with similar core structures (M_{13}).[52,53] Additionally, introducing Ni into the Ag_{13} icosahedral core will likely alter the system's spin-orbit coupling (SOC) characteristics, facilitating more efficient non-radiative relaxation pathways. As a result, the energy from excited states prefers to dissipate through nonradiative transitions rather than being emitted as photons (radiative transitions), thereby having the possibility of reducing PL intensity.

The theoretical absorption spectrum of $[NiAg_{28}BDT_{12}]^{4-}$ matches the experimental spectrum shape very well with peaks at 482 nm (2.57 eV), 424 nm (2.92 eV), and 312 nm (3.97 eV) as shown in Figure S15 (Supporting Information). In both the parent and doped cluster, there are a lot of single vertical excitations mixing into all the peaks. This is due to the small energy gaps between molecular orbitals. In the lower energy region, the absorption spectrum has a very broad weak peak across 1.5–2.5 eV as seen in Figure S16A (Supporting Information). The first dominant peak is made up of several vertical excitations; the one with the highest oscillator strength is at 2.57 eV with a value of 2.85 $\times 10^{-2}$ a.u. as documented in Tables S8 and S9 (Supporting Information). This excitation is dominated by a transition from H-32 to L+1, or an interband transition from a molecular orbital containing large contributions on the p atomic orbitals on sulfur transitioning to a superatomic D orbital created from a collective contribution from sp orbitals on Ag atoms in the core. The dominant transition that makes up the second peak at 2.92 eV is similar to the lower energy transition. The H-36 molecular orbital is primarily made up of p atomic contributions coming from the sulfur atoms in the ligands. This orbital transitions into a superatomic D orbital in the core of the nanocluster. As the electronic density in the occupied and virtual orbitals involved in both transitions do not overlap, there is ligand to metal charge transfer character as shown in **Figure 3**. The DFT methodology does not model charge transfer well at this level of theory as the exchange-correlation function chosen is too local in nature. Due to this, a long-range corrected exchange-correlation functional (LRCF) was used to try to model the electronic density more accurately. As shown in Figure S16B (Supporting Information), the results with the LRCF also have many vertical excitations mixing underneath the peaks. The two peaks at 2.49 and 2.85 eV in the parent cluster also show ligand to metal charge transfer character from an interband transition between the p orbitals on the sulfur atoms in the ligands to a superatomic D orbital in the core of the cluster. Even though there is a superatomic P nature with the Ni dopant, it does not change the behavior of the main absorption peak as the transitions do not originate from the occupied frontier orbitals.

The DFT calculations on $[NiAg_{28}BDT_{12}]^{4-}$ and $[Ag_{29}BDT_{12}]^{3-}$ both underestimate the experimentally observed emission energy of 1.90 eV (653 nm). The theoretical emission energies from the S_1 state are calculated at 1.18 and 1.08 eV for the dopant and parent cluster, respectively, with roughly the same radiative lifetime value of 12–13 µs. The theoretical emission from the T_1 state is higher than S_1 state in $[NiAg_{28}BDT_{12}]^{4-}$ with a value of 1.36 eV. Both, the parent cluster and the doped cluster change in the same way both geometrically and electronically upon excitation as seen in Table S10 (Supporting Information). Electronically, the HOMO gains 0.16 eV in energy upon excitation and the LUMO decreases by ≈0.30 eV as seen in Figure S17 (Supporting Information). Emission from the S_1 state

originates from a dominant HOMO→LUMO transition in both clusters.

The thermal stability of the NCs was monitored with respect to the change in absorption features upon heating. The absorbance spectra across a temperature range (25–145 °C) was recorded for Ag_{29} and $NiAg_{28}$ NCs as shown in Figure S8A (Supporting Information). For the Ag_{29} NCs, the absorbance spectra intensity versus temperature for both NCs decreased as temperature increased up to 135 °C. At 145 °C, the absorbance intensity jumped and became the highest intensity across all temperatures studied due to a change of Ag_{29} NCs into Ag nanoparticles (visible colors also reflect the same, Figure S8C, Supporting Information). On the other hand, $NiAg_{28}$ NCs show a systematic decrease in the absorbance intensity without significant modifications. These results exhibited clearly that the $NiAg_{28}$ NCs are more stable than pure Ag_{29} NCs. Thermogravimetric analysis (TGA) was performed under a nitrogen environment to determine the thermal stability for both, Ag_{29} and $NiAg_{28}$ NCs (see Figure S8B,D, Supporting Information). TGA determines the highest temperature at which the cluster remains stable.[3] The TGA curve begins to fall, indicating the temperature at which the ligands start to decompose. The Ag_{29} NCs were dissociated at 165 °C, which is lower than the dissociation point of $NiAg_{28}$ NCs (217 °C) by 52 °C, which indicates that the ligands of this Ni-doped Ag NC start to decompose at a higher temperature. The total weight loss of Ag_{29} and $NiAg_{28}$ NCs are 37.89% and 55.59%, respectively (Figure S8D, Supporting Information). A similar trend was seen in other doped nanoclusters.[3,12]

Considering the distinct differences between the parent NC and the Ni dopant in the electronic structure, optical absorption spectrum, and first electronically excited state, it is important to analyze other dopants and find trends. The monodopants Pt, Au, and Cu were analyzed in addition to Ni and compared with the parent cluster. To properly model these clusters, the first step was to find the most stable dopant position in the ground electronic state. In a similar way to the Ni dopant, Au was examined in the center, core, "tri" shell, and "tetra" shell positions. Cu and Pt have been studied experimentally and it has been shown that Pt prefers the center position[6,33] and Cu prefers a position in the shell.[14] Pt was therefore evaluated in the center position, and Cu was analyzed in the core, "tri" shell, and "tetra" shell positions to determine the preferred position. All in all, Ni, Au, and Pt prefer the center position of the core and Cu prefers the "tetra" position in the shell of the nanocluster; the relative energies at the BP86-D3/DZP level of theory can be seen in Table S11 (Supporting Information). It can be noted that the addition of a monodopant into this cluster will result in a smaller icosahedral core regardless of the dopant chosen, however, the overall size of the ligand shell has negligible changes with the different dopants, showing that the dopant changes the core but not the overall structure. The average bond distances in the ground state are shown in Tables S12 and S13 (Supporting Information).

All clusters have a superatomic electron count of 8 leading to a S^2P^6 configuration. The only NCs that collectively form three occupied superatomic P orbitals in the core are the Ni and Pt dopants. In these cases, there is still a large contribution from the p orbitals on the sulfur atoms, but the atomic d contribution from the dopant that is simultaneously mixing with the Ag to form the P orbitals in the HOMO, HOMO-1, and HOMO-2 as seen in Figure S18 (Supporting Information). There is hardly any contribution from the Au and Cu dopants in the frontier orbitals, which is different from the Ni and Pt dopants, which have very large contributions from the dopants integrating into the frontier orbitals. Ni and Pt have the largest HOMO–LUMO gaps at 1.62 and 1.68 eV respectively. The Au dopant has essentially the same HOMO–LUMO gap to the parent cluster at 1.48 eV, and the Cu dopant has a HOMO–LUMO gap of 1.41 eV. The difference in the electronic density between the different dopants in the HOMO and LUMO molecular orbitals can be seen in **Figure 4**.

Optically, all the NCs absorb light between 2.0–3.5 eV as seen in Figure S19 (Supporting Information). Similar to the Ni dopant, the Pt dopant has three strong peaks as opposed to just two in Au, Cu, and the parent NC. Despite the observed P orbitals in Ni and Pt, the electronic structure origins of the transitions of the main peaks in the absorption spectrum do not change much because the occupied P orbitals are not involved in the electronic transitions in the doped and parent clusters. The optical data at this level of theory can be seen in Tables S14 and S15 (Supporting Information). Unfortunately, even with a long-range corrected functional, the energy levels involved in the transitions form almost a manifold of states rather than the more discrete electronic state structure in all clusters.

The emission energies and radiative lifetimes from the optimized S_1 state for each doped cluster at the BP86-D3/DZP level of theory are shown in Table S16 (Supporting Information). All doped NCs underestimate the experimental emission energy just like the parent NC.[19] This could be an artifact of using DFT due to the charge transfer character in all the NCs. The largest emission energy is in the Pt-doped NC, followed by Ni, Au, Ag, and Cu NCs with values of 1.23, 1.18, 1.11, 1.08, and 1.06 eV respectively. The average bond distances in the optimized S_0 and S_1 states can be seen in Tables S17 and S18 (Supporting Information). In all the doped NCs, the HOMO–LUMO gaps get smaller as seen in Figure S20 (Supporting Information). In the Ni and Pt doped NCs, the superatomic P nature that was in the frontier orbitals of the optimized ground state change to frontier orbitals that are completely dependent upon contributions from the s and p orbitals in the sulfur and carbon atoms. This means that despite having a superatomic P nature in the ground state, the superatomic nature is lost upon excited state optimization. The emission mechanism is therefore similar in all clusters, which is dominated by a charge transfer mechanism from the ligands into the core of the Ag_{29-} NC.

The effect of Ni doping on the electrocatalytic performance of the cluster catalyst was evaluated by taking oxygen evolution as a model reaction. The oxygen evolution reaction (OER) involves the transfer of four electrons on the catalyst surface, with the overall reaction expressed as:

$$4OH^- \rightarrow 2H_2O + O_2 + 4e^- \text{ in alkaline medium} \quad (1)$$

The elementary steps are expressed as:

$$* + OH^- \rightarrow OH* + e^- \quad (2)$$

$$OH* + OH^- \rightarrow O* + H_2O + e^- \quad (3)$$

$$O* + OH^- \rightarrow OOH* + e^- \quad (4)$$

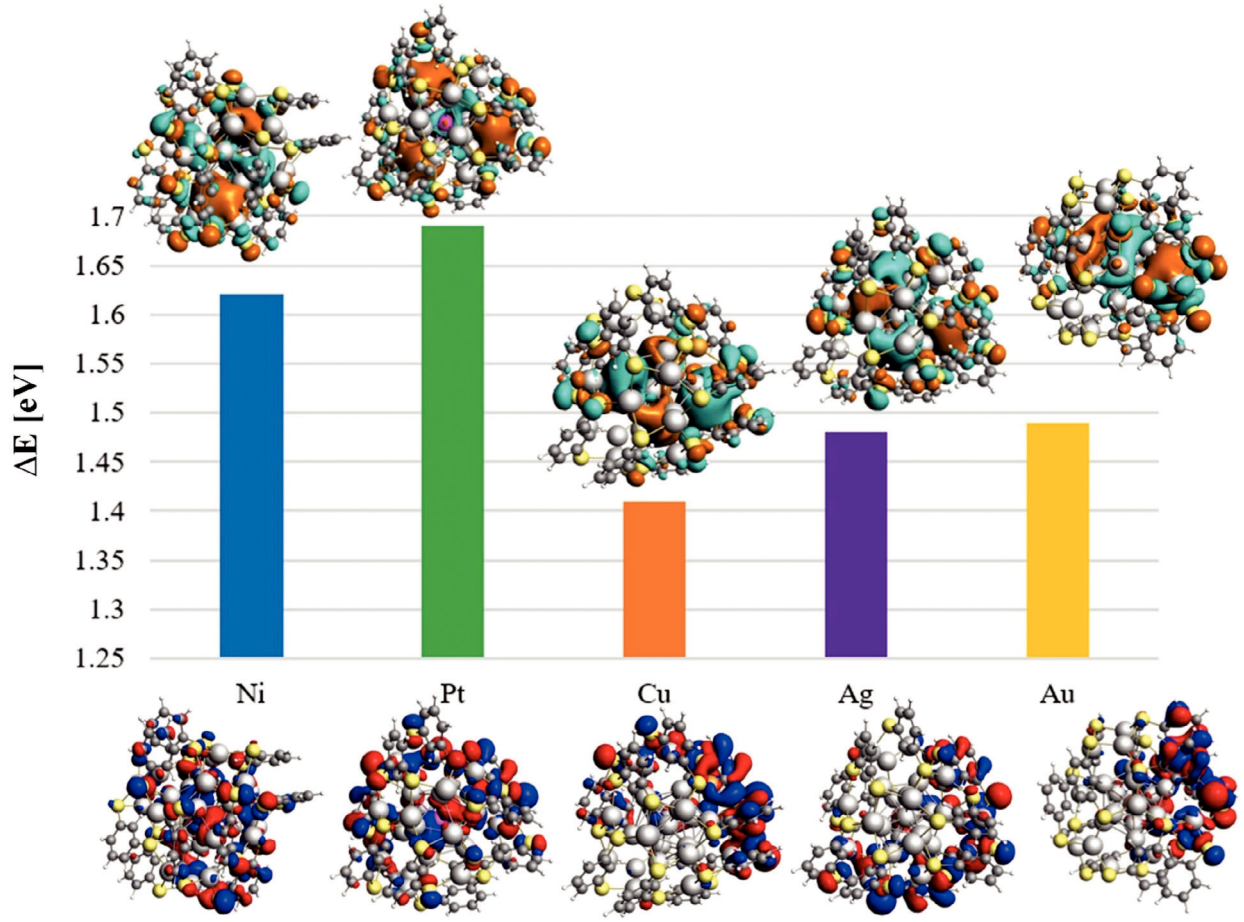

Figure 4. HOMO–LUMO gaps (eV) from the optimized ground state geometry at the BP86-D3/DZP level of theory where the electronic density of the HOMO is shown at the bottom of the graph and the LUMO is shown at the top of the graph for each doped cluster and the parent NC.

$$OOH * + OH^- \rightarrow * + O_2 + H_2O + e^- \quad (5)$$

where * donates the active site of the catalyst.

The OER activity of the $NiAg_{28}$ NCs was studied in 1 M KOH electrolyte and compared with bare Ag_{29} NCs (**Figure 5**). The linear sweep voltammogram (LSV) recorded using $NiAg_{28}$ NCs shows that the benchmark current density of 10 mA cm^{-2} was achieved at an overpotential of 417 mV; on the other hand, bare Ag_{29} NCs delivered very poor OER performance. This indicates the dominant role of Ni-doping on Ag NCs in enhancing electrocatalytic performance. The strong hump at ≈1.4 V (vs the reversible hydrogen electrode (RHE) potential) corresponds to the oxidation of Ni^{2+} to Ni^{3+}, forming nickel oxyhydroxide (NiOOH) during the oxidative sweep.[54] The in situ-generated metal oxyhydroxide (MOOH) is known to be the active species for OER.[55] The number of active sites per unit area or surface coverage (Γ) was estimated by integrating the charge associated with Ni^{2+} to Ni^{3+} oxidation, and it was found to be 1.21×10^{-5} mol cm^{-2}. In addition, the Tafel slope for $NiAg_{28}$ NCs was calculated to be 88.6 mV dec^{-1} (inset of Figure 5), and the small Tafel slope indicates facile charge transfer kinetics for OER.[56] The recyclability of the $NiAg_{28}$ NCs was tested by subjecting the electrode to repeated cyclic voltammograms (CVs), and an anodic shift of ≈60 mV was observed at the benchmark current density of 10 mA cm^{-2} after 500 catalytic cycles, demonstrating decent OER stability as shown in Section S1.3.9, Figure S9A,B (Supporting Information).

The incorporation of Ni into the Ag_{29} NCs plays a crucial role in enhancing the observed catalytic activity of the pristine Ag_{29} NCs. The volcano relationship suggests that Ag is relatively inert toward the OER, exhibiting poor catalytic activity, also observed in pristine Ag_{29} nanoclusters.[57,58] However, the Ni-doped Ag_{29} nanoclusters show a noticeable enhancement in the OER performance (Figure 5). This is probably due to Ni's significantly higher hydration enthalpy than Ag, though they exhibit similar electronegativity. This leads to the effective adsorption of OH^- ions at the catalyst's active sites.[59] Also, substituting a monovalent Ag atom with a bivalent Ni atom in the $NiAg_{28}$ cluster introduces an extra positive charge, further facilitating the adsorption of the O-atoms on the active sites and boosting the OER efficiency. Additionally, the spin state of Ni influences the catalytic performance of the catalyst as the spin state of the metal affects the sigma bonding between the e_g orbitals and oxygen-containing adsorbates, directly influencing the reaction rate and rate-determining steps (RDS) of the OER.[60–63] During the OER process, first, water molecules adsorb on the surface of the

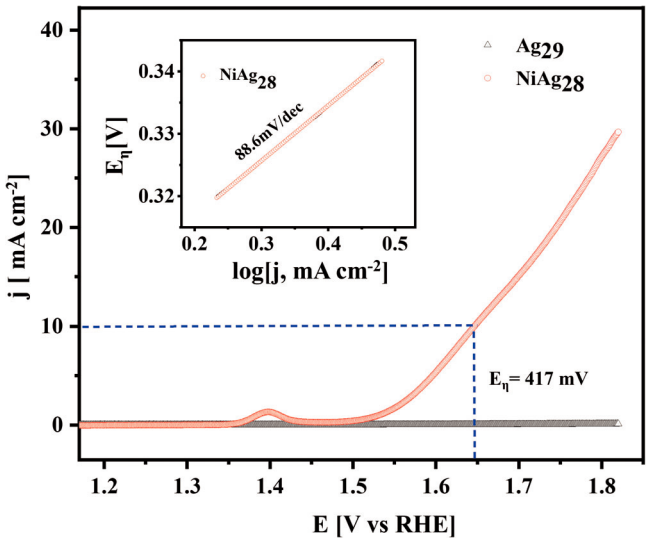

Figure 5. Electrochemical OER performance of $NiAg_{28}$ (red trace) compared to Ag_{29} (black trace) in 1 M KOH electrolyte: Linear sweep voltammetry (LSV) curves (LSV were recorded at a sweep rate of 5 mV s^{-1}), and the applied voltage was 417 mV for the $NiAg_{28}$ clusters when the current density was 10 mA cm^{-2}. The inset shows the Tafel plot of $NiAg_{28}$ NCs (with the potential E vs the potential of the RHE), which suggests a more favorable reaction kinetics.

catalyst's active sites and can be replaced by OH^- ions to form OH^* (* = catalyst) complex intermediates. The e_g orbital of the catalyst is directly oriented toward the OH species, forming a stronger sigma bond with the ($2p_x$+1s) orbitals of the OH than the overlap between the t_{2g} orbital of the catalyst with the ($2p_x$+1s) of OH. Thus, filling of the e_g orbital will provide a more accurate result in determining the energy gained by adsorption /desorption of OH on the catalyst surface and helping to determine the rate of the OER process.[62,64] In pristine Ag_{29} NCs, silver metals exist as Ag (0) ($d^{10}s^1$) or Ag (I) (d^{10}), both of which lack vacant orbitals to interact with the ($2p_x$ +1s) orbital of the OH species, hence exhibit poor activity in the OER process.

According to the XPS data, the nickel (Ni) atom in the doped Ag_{29} nanoclusters is in the +2-oxidation state and has two electrons e_g orbital (electronic configuration of $t_{2g}^6e_g^2$), which is partially filled. The linear sweep voltammogram (LSV) of OER shows a strong peak near 1.4 V versus RHE, corresponding to the oxidation of the Ni^{2+} to Ni^{3+} forming the NiOOH, which refers to the only active site of the OER process in the doped system. Here, half-filled e_g orbitals of Ni interact with the (2p+1s) orbital of the -OH firmly to form a strong Ni–OH intermediate, thus expediting the chain reaction of the OER process and effectively enhancing the OER performance of the Ni-doped AgNCs system (The d_{x2-y2} and d_{xy} are not involved in the hybridization process with the (2p+1s) of the OH because of symmetric conversation).

3. Conclusion

To summarize, Ni-doped Ag_{29} NCs were synthesized via a co-reduction approach. The formation of $NiAg_{28}(BDT)_{12}$ NCs was confirmed by ESI MS, IMS, and XPS. The experimental absorbance spectrum of the doped NCs with peaks at 482, 424, and 312 nm matches very well with the theoretical spectrum and confirms that it has the form of $[NiAg_{28}(BDT)_{12}]^{4-}$. Thermally, $NiAg_{28}(BDT)_{12}$ NCs demonstrate ultrastability compared to the pure $Ag_{29}(BDT)_{12}$ NCs by ≈67 °C based on TGA measurements. According to DFT, the most stable structure of $[NiAg_{28}(BDT)_{12}]^{4-}$ has an $Ag_{12}Ni$ icosahedral core with the Ni atom located at the center. DFT calculations further found that the open atomic d orbital contribution from the dopant aids in creating superatomic P-like HOMO–HOMO-2 molecular orbitals. The behavior of the main absorption peak of the pure cluster does not change in the doped cluster because the transitions do not originate from the occupied frontier orbitals. Emission is likely a result from fluorescence originating from the S_1 state. After S_1 optimization, however, the superatomic nature of the HOMO goes away. The emission mechanism is, therefore, dominated by a charge transfer mechanism from the ligands into the core of the Ag cluster regardless of dopant. Despite the change in the emission pathway, it is apparent that the Pt-doped cluster has the highest S_1 emission energy, followed by Ni, Au, and Cu. In addition, $[NiAg_{28}(BDT)_{12}]^{4-}$ exhibits enhanced electrochemical catalytic performance for OER as compared to pure $Ag_{29}(BDT)_{12}$NCs.

4. Experimental Section

The experimental section, including materials, methods, instruments, and characterization, was explained in detail in the Supporting Information file.

Supporting Information

Supporting Information is available from the Wiley Online Library or from the author.

Acknowledgements

A.A.A.A., S.H., and K.S. contributed equally to this work. This work was supported by the Deutsche Forschungsgemeinschaft (DFG grant PA 794_28-2 to W. J. P.). I.C. thanks the Scheme for Promotion of Academic and Research Collaboration (project ID: 3140); Science & Engineering Research Board (SERB) (project id: SRG/2022/000135) and SRIC, IIT Kharagpur (Project code: DLR) for the support. A.A. was supported by the IIE Scholar Rescue Fund (IIE-SRF). S.H. and C.M.A. were supported by the National Science Foundation (CHE-1905048) of the United States. K.S. thanks PMRF for his fellowship. The computing for this work was performed on the Beocat Research Cluster at Kansas State University, which is funded in part by NSF grants CHE-1726332, CNS-1006860, EPS-1006860, and EPS-0919443.

Open access funding enabled and organized by Projekt DEAL.

Conflict of Interest

The authors declare no conflict of interest.

Data Availability Statement

The data that support the findings of this study are available in the supplementary material of this article.

Keywords

DFT study, electrochemical properties, nanoclusters, optical properties

Received: September 8, 2024
Revised: October 22, 2024
Published online: November 24, 2024

[1] R. Jin, C. Zeng, M. Zhou, Y. Chen, *Chem. Rev.* **2016**, *116*, 10346.
[2] E. Khatun, P. Chakraborty, B. R. Jacob, G. Paramasivam, M. Bodiuzzaman, W. A. Dar, T. Pradeep, *Chem. Mater.* **2019**, *32*, 611.
[3] X. Kang, H. Abroshan, S. Wang, M. Zhu, *Inorg. Chem.* **2019**, *58*, 11000.
[4] X. Liu, Y. Tang, L. Chen, L. Wang, Y. Liu, Z. Tang, *Int. J. Hydrogen Energy* **2024**, *53*, 300.
[5] X. Lin, W. Ma, K. Sun, B. Sun, X. Fu, X. Ren, C. Liu, J. Huang, *J. Phys. Chem. Lett.* **2021**, *12*, 552.
[6] M. S. Bootharaju, S. M. Kozlov, Z. Cao, M. Harb, M. R. Parida, M. N. Hedhili, O. F. Mohammed, O. M. Bakr, L. Cavallo, J.-M. Basset, *Nanoscale* **2017**, *9*, 9529.
[7] G. Soldan, M. A. Aljuhani, M. S. Bootharaju, L. G. AbdulHalim, M. R. Parida, A. H. Emwas, O. F. Mohammed, O. M. Bakr, *Angew. Chem.* **2016**, *128*, 5843.
[8] D. Mishra, V. Lobodin, C. Zhang, F. Aldeek, E. Lochner, H. Mattoussi, *Phys. Chem. Chem. Phys.* **2018**, *20*, 12992.
[9] X. Zou, S. He, X. Kang, S. Chen, H. Yu, S. Jin, D. Astruc, M. Zhu, *Chem. Sci.* **2021**, *12*, 3660.
[10] X.-Y. Xie, P. Xiao, X. Cao, W.-H. Fang, G. Cui, M. Dolg, *Angew. Chem., Int. Ed.* **2018**, *57*, 9965.
[11] X. Lin, C. Liu, K. Sun, R. Wu, X. Fu, J. Huang, *Nano Res.* **2019**, *12*, 309.
[12] X. Kang, M. Zhou, S. Wang, S. Jin, G. Sun, M. Zhu, R. Jin, *Chem. Sci.* **2017**, *8*, 2581.
[13] J. Yan, H. Su, H. Yang, S. Malola, S. Lin, H. Häkkinen, N. Zheng, *J. Am. Chem. Soc.* **2015**, *137*, 11880.
[14] M. S. Bootharaju, C. P. Joshi, M. R. Parida, O. F. Mohammed, O. M. Bakr, *Angew. Chem.* **2016**, *128*, 934.
[15] K. R. Krishnadas, A. Baksi, A. Ghosh, G. Natarajan, A. Som, T. Pradeep, *Acc. Chem. Res.* **2017**, *50*, 1988.
[16] R. Jin, S. Zhao, Y. Xing, R. Jin, *CrystEngComm* **2016**, *18*, 3996.
[17] E. Khatun, T. Pradeep, *Atomically Precise Metal Nanoclusters*, (Ed: T. Pradeep), Elsevier, Amsterdam/New York **2023**, pp. 393–426.
[18] S. A. Shah, K.-J. Hu, M. Naveed, S. N. A. Shah, S. Hu, S. Lu, F. Song, *Mater. Res. Express* **2019**, *7*, 016506.
[19] J. Yang, R. Pang, D. Song, M.-B. Li, *Nanoscale Adv.* **2021**, *3*, 2411.
[20] X. Liu, T. Ki, G. Deng, S. Yoo, K. Lee, B.-H. Lee, T. Hyeon, M. S. Bootharaju, *Nanoscale* **2024**, *16*, 11090.
[21] Y. Zhou, W. Gu, R. Wang, W. Zhu, Z. Hu, W. Fei, S. Zhuang, J. Li, H. Deng, N. Xia, *Nano Lett.* **2024**, *24*, 2226.
[22] P. Bose, K. K. Ramankutty, P. Chakraborty, E. Khatun, T. Pradeep, *Nanoscale* **2024**, *16*, 1446.
[23] Y. Jin, C. Zhang, X.-Y. Dong, S.-Q. Zang, T. C. W. Mak, *Chem. Soc. Rev.* **2021**, *50*, 2297.
[24] I. Chakraborty, T. Pradeep, *Chem. Rev.* **2017**, *117*, 8208.
[25] H. Fakhouri, E. Salmon, X. Wei, S. Joly, C. Moulin, I. Russier-Antoine, P.-F. Brevet, X. Kang, M. Zhu, R. Antoine, *J. Phys. Chem. C* **2022**, *126*, 21094.
[26] E. Khatun, T. Pradeep, *ACS Omega* **2021**, *6*, 1.
[27] A. Baksi, E. K. Schneider, P. Weis, I. Chakraborty, O. Fuhr, S. Lebedkin, W. J. Parak, M. M. Kappes, *ACS Nano* **2020**, *14*, 15064.
[28] X. Lin, H. Cong, K. Sun, X. Fu, W. Kang, X. Wang, S. Jin, R. Wu, C. Liu, J. Huang, *Nano Res.* **2020**, *13*, 366.
[29] M. S. Bootharaju, S. M. Kozlov, Z. Cao, A. Shkurenko, A. M. El-Zohry, O. F. Mohammed, M. Eddaoudi, O. M. Bakr, L. Cavallo, J.-M. Basset, *Chem. Mater.* **2018**, *30*, 2719.
[30] E. Khatun, P. Chakraborty, B. R. Jacob, G. Paramasivam, M. Bodiuzzaman, W. A. Dar, T. Pradeep, *Chem. Mater.* **2020**, *32*, 611.
[31] M. K. Debe, *Nature* **2012**, *486*, 43.
[32] J. Zhu, L. Hu, P. Zhao, L. Y. S. Lee, K.-Y. Wong, *Chem. Rev.* **2020**, *120*, 851.
[33] K. Kwak, D. Lee, *Acc. Chem. Res.* **2018**, *52*, 12.
[34] X. Zhu, L. Chen, Y. Liu, Z. Tang, *Polyoxometalates* **2023**, *2*, 9140031.
[35] H. Shen, Q. Zhu, J. Xu, K. Ni, X. Wei, Y. Du, S. Gao, X. Kang, M. Zhu, *Nanoscale* **2023**, *15*, 14941.
[36] L. G. AbdulHalim, M. S. Bootharaju, Q. Tang, S. Del Gobbo, R. G. AbdulHalim, M. Eddaoudi, D. Jiang, O. M. Bakr, *J. Am. Chem. Soc.* **2015**, *137*, 11970.
[37] J.-Y. Wang, Y.-K. Li, X. Jing, P. Luo, X.-Y. Dong, S.-Q. Zang, *ACS Mater. Lett.* **2022**, *4*, 960.
[38] X. Gao, S. Dong, L. Fu, Y. Xu, J. Jia, G. Zou, *J. Phys. Chem. C* **2021**, *125*, 22078.
[39] A. Ghosh, D. Ghosh, E. Khatun, P. Chakraborty, T. Pradeep, *Nanoscale* **2017**, *9*, 1068.
[40] Y. Zeng, S. Havenridge, M. Gharib, A. Baksi, K. L. D. M. Weerawardene, A. R. Ziefuß, C. Strelow, C. Rehbock, A. Mews, S. Barcikowski, M. M. Kappes, W. J. Parak, C. M. Aikens, I. Chakraborty, *J. Am. Chem. Soc.* **2021**, *143*, 9405.
[41] J. P. Perdew, *Phys. Rev. B* **1986**, *33*, 8822.
[42] A. D. Becke, *Phys. Rev. A* **1988**, *38*, 3098.
[43] S. Grimme, S. Ehrlich, L. Goerigk, *J. Comput. Chem.* **2011**, *32*, 1456.
[44] E. Van Lenthe, E. J. Baerends, *J. Comput. Chem.* **2003**, *24*, 1142.
[45] G. te Velde, F. M. Bickelhaupt, E. J. Baerends, C. Fonseca Guerra, S. J. A. van Gisbergen, J. G. Snijders, T. Ziegler, *J. Comput. Chem.* **2001**, *22*, 931.
[46] E. Khatun, A. Ghosh, P. Chakraborty, P. Singh, M. Bodiuzzaman, P. Ganesan, G. Nataranjan, J. Ghosh, S. K. Pal, T. Pradeep, *Nanoscale* **2018**, *10*, 20033.
[47] J. V. Rival, P. Mymoona, R. Vinoth, A. M. V. Mohan, E. S. Shibu, *ACS Appl. Mater. Interfaces* **2021**, *13*, 10583.
[48] J. Fu, S. Cao, J. Yu, *J. Materiomics* **2015**, *1*, 124.
[49] Y. Xu, X. Liu, Y. Zheng, C. Li, K. W. K. Yeung, Z. Cui, Y. Liang, Z. Li, S. Zhu, S. Wu, *Bioact. Mater.* **2021**, *6*, 1575.
[50] H. Shen, J. Xu, Z. Fu, X. Wei, X. Kang, W. Shi, M. Zhu, *Angew. Chem., Int. Ed.* **2024**, *63*, e202317995.
[51] M. Mitsui, A. Uchida, *Nanoscale* **2024**, *16*, 3053.
[52] X. Kang, X. Wei, S. Jin, Q. Yaun, X. Laun, Y. Pei, S. Wang, M. Zhu, R. Jin, *Proc. Natl. Acad. Sci. USA* **2019**, *116*, 18834.
[53] J. P. Herbert, M. A. Tofanelli, C. J. Ackerson, K. L. Knappenberger Jr., *J. Phys. Chem. C* **2021**, *125*, 7267.
[54] T. Li, Y. Chen, Z. Tang, Z. Liu, C. Wang, *Electrochim. Acta* **2019**, *307*, 403.
[55] Z. Angeles-Olvera, A. Crespo-Yapur, O. Rodríguez, J. L. Cholula-Díaz, L. M. Martínez, M. Videa, *Energies* **2022**, *15*, 1609.
[56] S. Gratious, A. Karmakar, D. Kumar, S. Kundu, S. Chakraborty, S. Mandal, *Nanoscale* **2022**, *14*, 7919.
[57] B. You, M. T. Tang, C. Tsai, F. Abild-Pedersen, X. Zheng, H. Li, *Adv. Mater.* **2019**, *31*, 1807001.
[58] C. Deng, R. He, W. Seng, M. Li, *Phys. Chem. Chem. Phys.* **2019**, *21*, 18589.
[59] P. Hota, S. Bose, D. Dinda, P. Das, U. K. Ghorai, S. Bag, S. Mondal, S. K. Saha, *ACS Omega* **2018**, *3*, 17070.
[60] Y. Zhang, Q. Wu, J. Z. Y. Seow, Y. Jia, X. Ren, Z. J. Xu, *Chem. Soc. Rev.* **2024**, *53*, 8123.
[61] Z. Wang, S. Shen, Z. Lin, W. Tao, Q. Zhang, F. Mang, L. Gu, W. Zhong, *Adv. Func. Mater.* **2022**, *32*, 2112832.
[62] J. Suntivich, H. A. Gasteiger, N. Yabuuchi, H. Nakanishi, J. B. Goodenough, Y. Shao-Horn, *Nat. Chem.* **2011**, *3*, 546.
[63] Y. Li, M. Yaun, H. Yang, K. Shi, Z. Sun, H. Li, C. Nan, G. Sun, *Appl. Catal., B* **2023**, *323*, 122167.
[64] J. O. M. Bockris, T. Otagawa, *J. Electrochem. Soc.* **1984**, *131*, 290.